Supplementary Information

W.H. Evers,* B. de Nijs,* L. Filion,† S. Castillo,* M. Dijkstra,† and D. Vanmaekelbergh*
Debye Institute for Nanomaterials Science, Utrecht University, The Netherlands

I. ADDITIONAL EXPERIMENTAL PLOTS

size ratio (effective)	Diameter NC (nm)		BNSLs obtained	2D surface coverage (%)
	Large	*Small*		
0.53	11.0 (PbSe)	5.8 (CdSe)	AlB_2	60
			$NaZn_{13}$	1
			Single component	10
0.56	10.3 (PbSe)	5.8 (CdSe)	AlB_2	10
			$NaZn_{13}$	60
			Single component	10-20
0.59 (2) T=70 °C	9.8 (PbSe)	5.8 (CdSe)	AlB_2	<1
			$NaZn_{13}$	5-15
			Single component	40-60
0.59 (2) T=20 °C	9.8 (PbSe)	5.8 (CdSe)	AlB_2	<1
			$NaZn_{13}$	10-20
			Single component	5-15
0.6	9.61 (PbSe)	5.8 (CdSe)	AlB_2	<1
			$NaZn_{13}$	<1
			unknown	<1
			Single component	10-80
0.62	9.43 (PbSe)	5.8 (CdSe)	AlB_2	<1
			$NaZn_{13}$	<1
			unknown	<1
			Single component	20-60
0.65	8.88 (PbSe)	5.8 (CdSe)	$MgZn_2$	<1
			$CaCu_5$	<1
			Single component	
0.72	8.09 (PbSe)	5.8 (CdSe)	$MgZn_2$	<1
			Single component	>50
0.73	8.0 (PbSe)	5.8 (CdSe)	$MgZn_2$	25
			$CaCu_5$	1
			Single component	40-60
0.75 T=70°C	7.76 (PbSe)	5.8 (CdSe)	$MgZn_2$	10-15
			CsCl	<1-5
			Single component	20-50
0.75 T=20°C	7.76 (PbSe)	5.8 (CdSe)	$MgZn_2$	<1-7
			CsCl	10-15
			Single component	20-40
0.79	7.37 (PbSe)	5.8 (CdSe)	$MgZn_2$	<1
			$CaCu_5$	<1
			Single component	20-80
0.8	7.23 (PbSe)	5.8 (CdSe)	$MgZn_2$	<1
			$CaCu_5$	<1
			Single component	30-80

TABLE 1: Overview of the superlattices obtained by solvent evaporation from binary suspensions of semiconductor nanocrystals, i.e. combinations of PbSe NC and CdSe NC with varying size ratio $\gamma = \sigma_S/\sigma_L$, where $\sigma_{S(L)}$ is the diameter of the small (large) particles. Solvent evaporation was performed at 70°C (unless otherwise stated). The relative importance of the different structures that are formed are expressed in maximum % surface coverage.

*Condensed Matter and Interfaces
†Soft Condensed Matter

size ratio (effective)	Diameter NC (nm)		Crystal structure	2D surface coverage (%)
	Large	*Small*		
0.47	11.0 (PbSe)	5.2 (Au)	NaCl	1-5
			CuAu	<1
			Cu_3Au	<1
			$CaCu_5$	<1
			Single component	10-50
0.53	9.8 (PbSe)	5.2 (Au)	CuAu	<1
			Single component	10-20
0.55	9.49 (PbSe)	5.2 (Au)	CuAu	<1
			Single component	10-20
0.57	9.8 (PbSe)	5.58 (Au)	$NaZn_{13}$	<1
			Single component	1-20
0.59	11.0 (PbSe)	6.59 (Au)	AlB_2	<1
			Single component	10-50
0.61	9.49 (PbSe)	5.8 (Au)	AlB_2	<1
			Single component	10-50
0.64	9.8 (PbSe)	6.29 (Au)	CuAu	1-5
			Single component	30-50
0.68	11.0 (PbSe)	7.51 (Au)	AlB_2	<1
			Single component	10-50
0.74	6.98 (PbSe)	5.2 (Au)	CsCl	20-30
			Single component	10-30
0.83	6.98 (PbSe)	5.8 (Au)	CsCl	1-10
			$CaCu_5$	1-5
			Single component	10-50
0.86	8.1 (Au)	6.98 (PbSe)	CsCl	<1
			Single component	30-50

TABLE 2: Overview of the superlattices formed from a PbSe NC / Au NC suspension for different size ratios γ. The relative importance of the structures that are formed are expressed as maximum % coverage of the total surface area examined. The solvent evaporation was performed at 70°C.

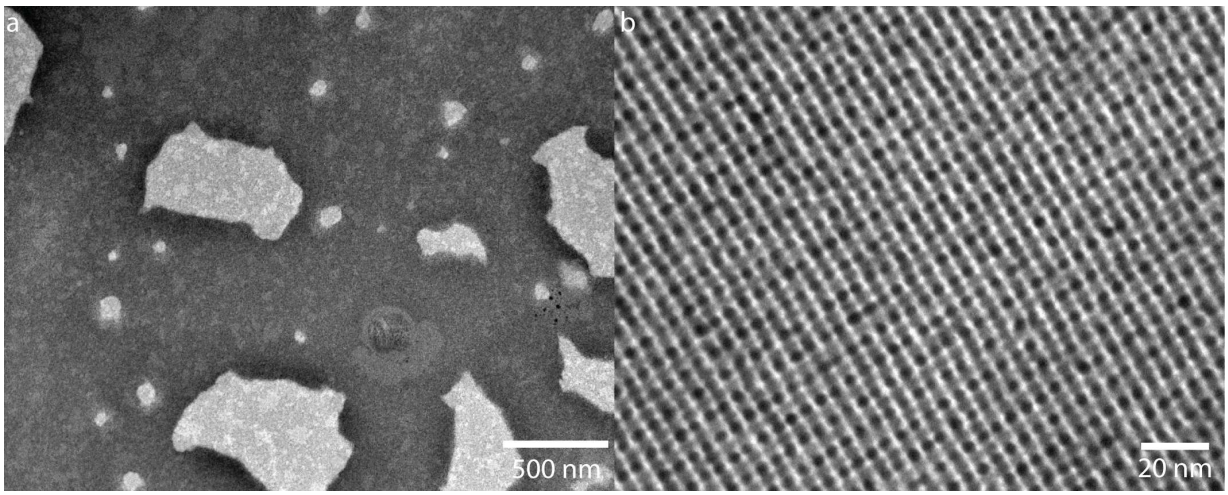

FIG. S1: Binary and single-component superlattices obtained from a suspension of PbSe nanocrystals (7.0 nm effective diameter) and Au nanocrystals (5.2 nm effective diameter) at a size ratio $\gamma = 0.74$. (a) overview of the TEM grid with single component domains of PbSe and Au NCs, binary domains PbSe(Au), iso-structural with CsCl. (b) detailed TEM image showing a binary PbSe(Au) superlattice with CsCl structure.

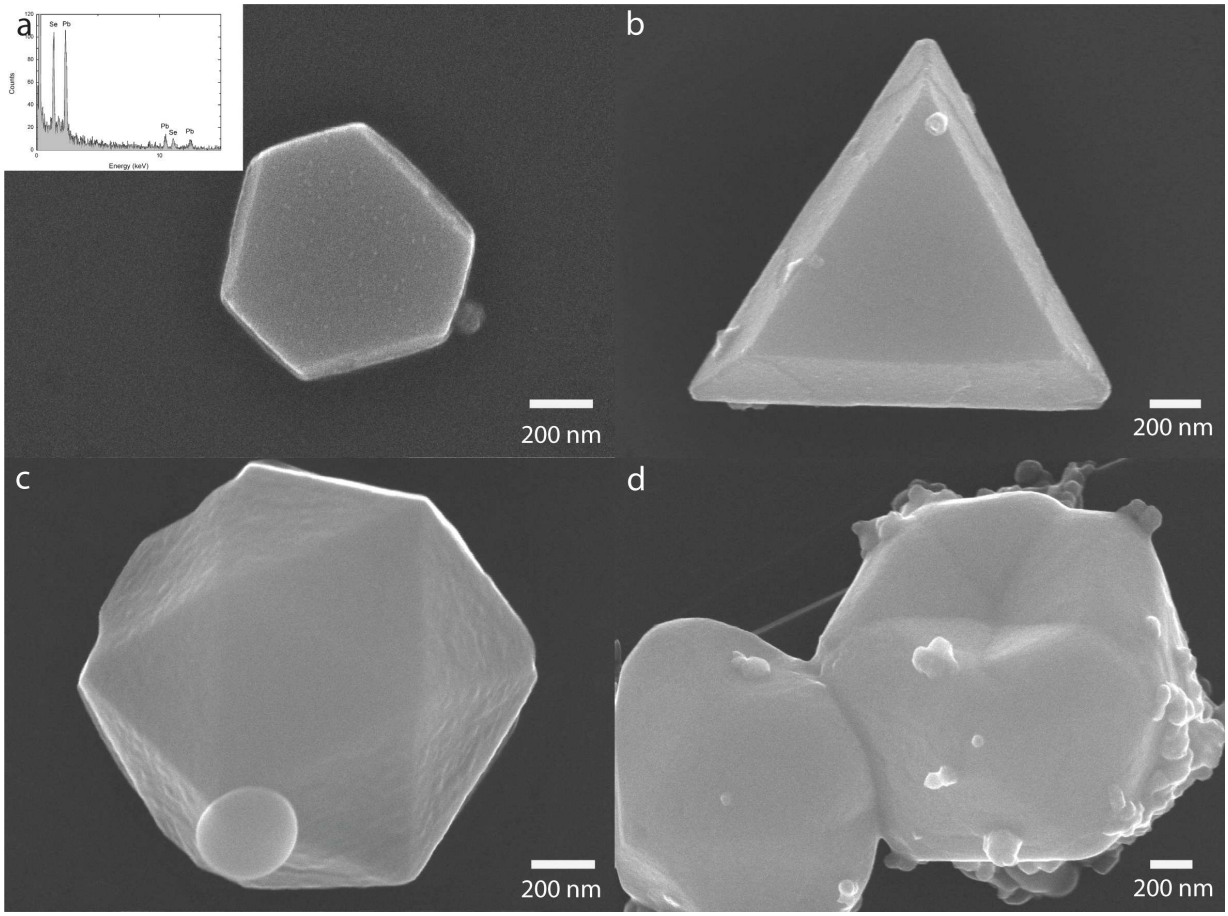

FIG. S2: Crystals obtained due to addition of a non-solvent to a binary suspension consisting of large PbSe NCs and smaller CdSe or Au NCs. The size ratio γ was varied between 0.53 and 0.98. Only single-component superlattices consisting of the larger PbSe NC were observed. Different crystal shapes are found: (a) hexagonal platelet, (b) triangular platelet, (c) icosahedron, (d) collapsed icosahedrons. In the inset of (a), an EDX spectrum is given, indicating the presence of PbSe NCs only.

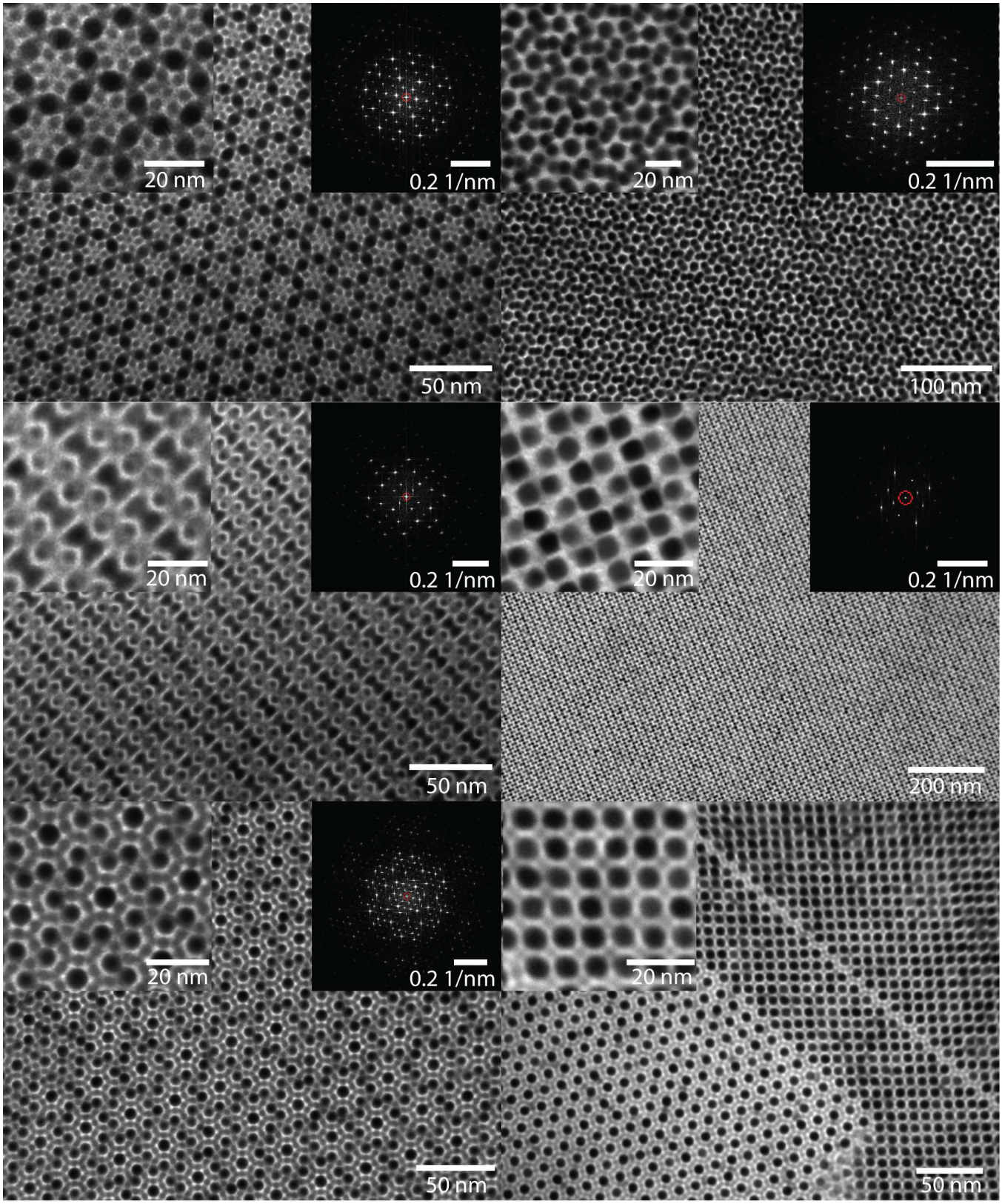

FIG. S3: Unknown binary superlattices obtained from PbSe and CdSe NCs at a size ratio γ between 0.60-0.63. In the inset of each of the images, a zoom in of the TEM pictures of the crystal structure and a Fourier transform are presented.

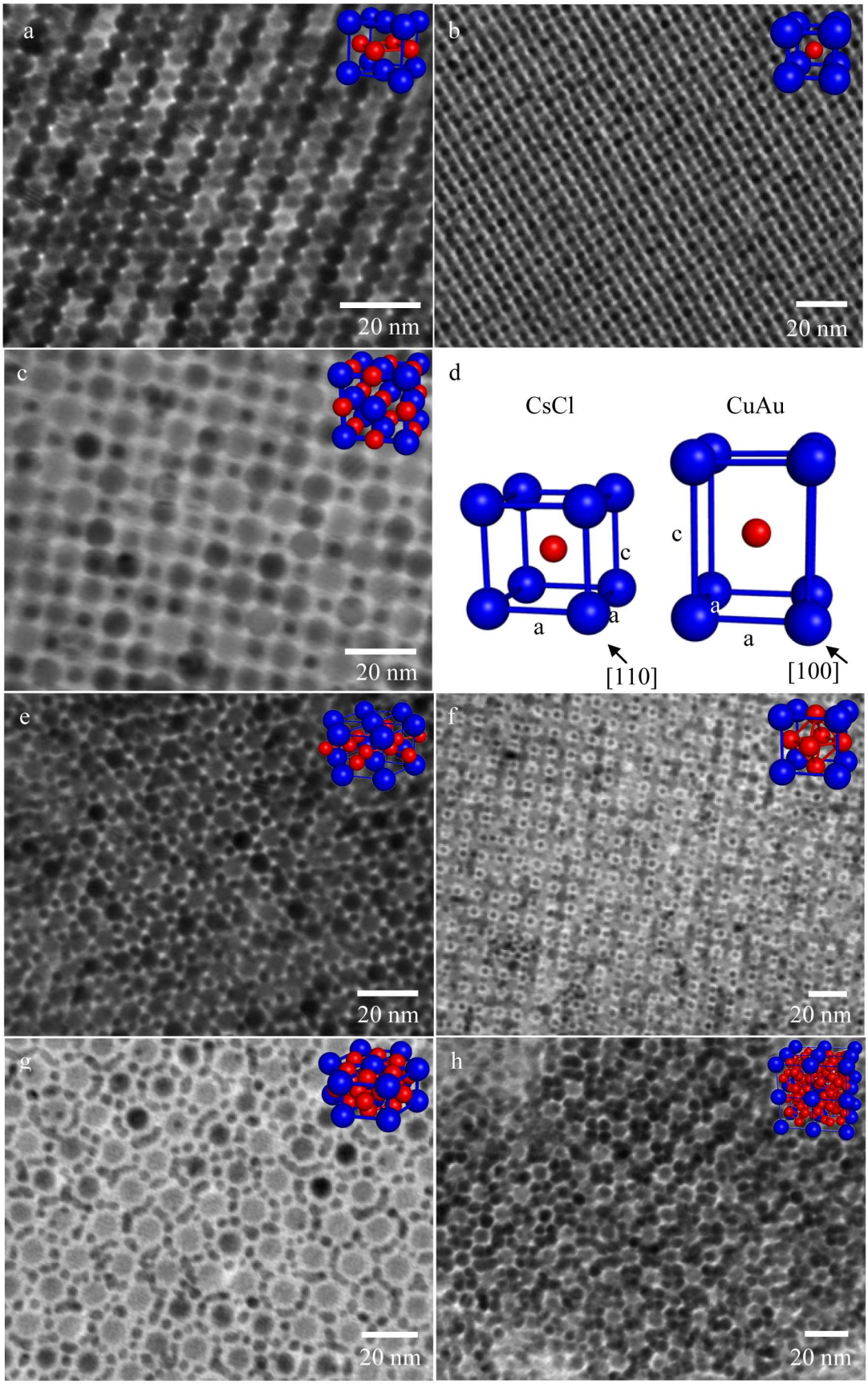

FIG. S4: Binary superlattices obtained by colloidal crystallization at 70°C from suspensions of PbSe and Au nanocrystals. (a)-(c) Binary superlattices with AB stoichiometry (a) CuAu structure ($\gamma = 0.53$), (b) CsCl structure ($\gamma = 0.74$), (c) NaCl structure ($\gamma = 0.47$). (d) Cartoon showing the difference between CsCl and CuAu structure. The CsCl structure consists of a cubic lattice of the large particles where the axes of the unit cell are all equal, while the CuAu structure has one prolonged axis. (e) AlB_2 structure ($\gamma = 0.61$). (f) Cu_3Au ($\gamma = 0.47$). (g) $CaCu_5$ structure ($\gamma = 0.83$). (h) $NaZn_{13}$ structure ($\gamma = 0.57$).

II. BINARY HARD SPHERE MIXTURES

A. Summary of Theoretical Results

In Table 3 we list all the binary crystal structures which are predicted to be stable in the phase diagrams of binary hard-sphere mixtures obtained from full free-energy calculations for various size ratios $\gamma = \sigma_S/\sigma_L$ where $\sigma_{S,L}$ is the diameter of the small and large hard spheres, respectively [1–6].

Size Ratio (γ)	Stable Crystal Structures	Reference
0.033	fcc with disordered small	1
0.05	fcc with disordered small	1
0.1	fcc with disordered small	1
0.2	fcc with disordered small	1
0.414	NaCl	2
0.45	NaCl and AlB_2	2
0.50	AlB_2	3
0.54	AlB_2 and ico-AB_{13}	3
0.58	AlB_2 and ico-AB_{13}	3, 4
0.59	AlB_2 and ico-AB_{13}	3
0.60	AlB_2 and ico-AB_{13}	3
0.61	AlB_2 and ico-AB_{13}	3
0.625	ico-AB_{13}	3
0.74	only fcc_L and fcc_S	5
0.76	Laves Phases ($MgZn_2$, $MgCu_2$, $MgNi_2$)	5
0.80	Laves Phases ($MgZn_2$, $MgCu_2$, $MgNi_2$)	5
0.82	Laves Phases ($MgZn_2$, $MgCu_2$, $MgNi_2$)	5
0.84	Laves Phases ($MgZn_2$, $MgCu_2$, $MgNi_2$)	5
0.85	eutectic solidsolution	6
0.875	eutectic solidsolution	6
0.90	azeotropic	6
0.92	azeotropic	6
0.9425	azeotropic	6
0.95	fcc solid solution (spindle)	6

TABLE 3: A list of all the structures which have been shown to be stable in hard-sphere systems as a function of the size ratio γ.

B. Binary Hard-Sphere Mixtures Theory

From thermodynamics, the Helmholtz free energy F of a system consisting of N particles in a volume V, and at temperature T is given by

$$F = U - TS \tag{1}$$

where U is the potential energy, and S is the entropy. For a system consisting of hard spheres the pair potential is given by

$$V_{\rm HS}(r_{ij}, \sigma_i, \sigma_j) = \begin{cases} 0 & r_{ij} > (\sigma_i + \sigma_j)/2 \\ \infty & r_{ij} \leq (\sigma_i + \sigma_j)/2 \end{cases} \tag{2}$$

where r_{ij} is the distance between particles i and j, and σ_i is the diameter of particle i. Since the Boltzmann weight is zero for configurations that contain particle overlaps, the free energy is determined solely by the entropy. (The potential energy contribution to the free energy for all configurations without overlaps is simply zero, hence only the entropic term is left.)

One method of calculating the exact free energy for a general system, such as hard-sphere mixtures, is thermodynamic integration. In this case, it is assumed that there exists a reference system for which we can calculate the free energy analytically. For example, for liquids often the ideal gas is used and for crystals, the Einstein crystal can serve as the reference system. If the potential energy of the reference system is given by U_R and the potential energy of

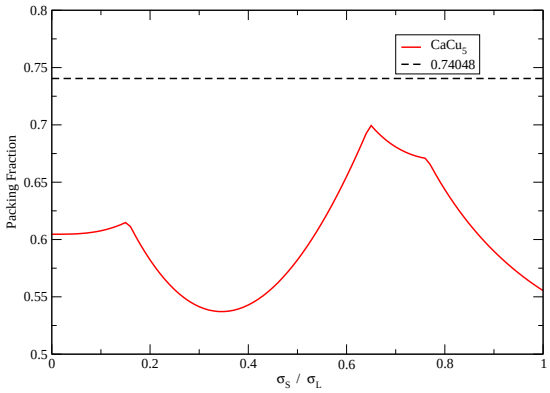

FIG. S5: Maximum packing fraction of $CaCu_5$ as a function of the size ratio σ_S/σ_L.

our true system of interest is denoted U_T then it is possible to define a new (fictitious) potential energy

$$U(\lambda) = (1-\lambda)U_T + \lambda U_R, \tag{3}$$

which is now a function of a coupling parameter λ, which varies between 0 and 1. Note that this function has the property that when $\lambda = 0$ it reduces to our system of interest, and when $\lambda = 1$ it reduces to the reference system. The free-energy difference between the reference and the system of interest can be determined exactly, see Ref. 7, and is given by

$$F(\lambda=1) - F(\lambda=0) = \int_{\lambda=0}^{\lambda=1} d\lambda \left\langle \frac{\partial U(\lambda)}{\partial \lambda} \right\rangle_\lambda . \tag{4}$$

Thus, to calculate the free energy exactly we simply need to determine $\langle \partial U(\lambda)/\partial\lambda \rangle_\lambda$ as a function of λ. Such an average can be determined using a Monte Carlo simulation. Additionally, after the Helmholtz free energy is known, all other relevant thermodynamic quantities (such as the Gibbs free energy) can then be obtained.

Once the free energies are known, techniques such as common tangent constructions are used to determine the phase diagrams, and thus, the stability of various candidate phases. Such methods make use of the fact that the temperature, pressure and chemical potential of all the species must be equal in the coexisting phases when the system is in thermodynamic equilibrium. Equivalently, the system always chooses the state with the lowest total Gibbs free energy. Specifically, the system will choose a linear combination of phases such that the total Gibbs free energy is minimized.

C. Stability of $CaCu_5$

To study the stability of the $CaCu_5$ structure as a candidate crystal structure for a binary hard-sphere system we first examined the maximum packing fraction of the structure as a function of the size ratio γ of the particles. A plot of the maximum packing fraction is shown in Fig. S5.

From Fig. S5 we notice that $CaCu_5$ is most likely to be stable for a size ratio range $0.64 - 0.70$ as the highest possible packing fraction lies within this range. In order to determine whether or not $CaCu_5$ is stable, we calculate the Gibbs free-energy of $CaCu_5$ and compare it with that of phase separated single-component fcc crystals. To calculate the Gibbs free energy of $CaCu_5$ we used the Frenkel-Ladd Einstein integration method as described in Ref. 8 and in Sec. IIB. For the single-component fcc crystals we used the free energy expressions from Ref. 9. For size ratios 0.64, and 0.70, we find that the phase separated fcc phase has a lower Gibbs free energy than that of the $CaCu_5$ structure, indicating that $CaCu_5$ is not thermodynamically stable for binary hard-sphere mixtures.

III. INTERACTIONS

In order to make predictions for the phase behaviour of complex fluids, one often resorts to simplified models in which the degrees of freedom of the microscopic species (solvent, polymer) are formally integrated out so that the macroscopic constituents interact via effective interactions. This is a well-trodden pathway in statistical physics

and has been applied successfully in colloidal science [1, 10–12]. By integrating out the degrees of freedom of the microscopic species in the partition function, one can derive a formal expression for the effective Hamiltonian for the macroscopic species, which include many-body interactions. If the effective pair interactions are sufficiently short-ranged, three- and higher body effective interactions can be neglected and pairwise additivity of the effective pair interactions can be assumed. In the case examined in this paper, particularly in the case of semiconductor nanoparticle mixtures, both the steric interaction and the screened Van der Waals interactions, are short ranged. As a result, pairwise interaction potentials are expected to be a good first approximation for the effective interaction between nanoparticles. In this section, we consider a pairwise potential consisting of a contribution from a Van der Waals (VdWs) interaction between the cores, a steric interaction between the capping ligands, and a hard-sphere replusion between the cores. The effective potential is given by

$$\beta V_{\rm eff}(r_{ij},\sigma_i,\sigma_j) = \beta V_{\rm vdw}(r_{ij},\sigma_i,\sigma_j) + \beta V_{\rm steric}(r_{ij},\sigma_i,\sigma_j) + \beta V_{\rm HS}(r_{ij},\sigma_i,\sigma_j), \tag{5}$$

where r_{ij} is the distance between the center of mass of two nanoparticles i and j, σ_i is the diameter of particle i, $V_{\rm HS}(r_{ij},\sigma_i,\sigma_j)$ is given by Eq. 2, $\beta = 1/k_BT$, k_B is Boltzmann's constant and T is the temperature. We assume that the Van der Waals interaction between the capping layers can be neglected for a monolayer protected nanocrystal in a good solvent.

A. Van der Waals

The Van der Waals interaction between two core-shell particles labelled i and j at distance r_{ij} with diameters $\sigma_{i(j)}$ and Hamaker constant A is given by [13, 14]

$$\beta V_{\rm vdw}(r_{ij},\sigma_i,\sigma_j) = -\frac{\beta A}{12}\left[\frac{S_{ij}}{D_{ij}\left(1+\frac{D_{ij}}{(\sigma_i+\sigma_j)}\right)} + \frac{1}{1+\frac{D_{ij}}{S_{ij}}+\frac{D_{ij}^2}{\sigma_i\sigma_j}} + 2\ln\left(\frac{D_{ij}\left(1+\frac{D_{ij}}{(\sigma_i+\sigma_j)}\right)}{S_{ij}\left(1+\frac{D_{ij}}{S_{ij}}+\frac{D_{ij}^2}{\sigma_i\sigma_j}\right)}\right)\right], \tag{6}$$

where $S_{ij} = \sigma_i\sigma_j/(\sigma_i+\sigma_j)$ and $D_{ij} = r_{ij} - (\sigma_i+\sigma_j)/2$.

For the Hamaker constant, we consider gold-gold interactions, gold-semiconductor interactions, and semiconductor-semiconductor interactions. For the gold-gold interaction we let A=3 eV. We note that values for the gold-gold interaction are found between approximately 1.1 and 3 eV [15–18], where we note that some of the literature has used the fact that the gold-gold Hamaker constant is approximately equal to the silver-silver Hamaker constant. The CdSe-CdSe Hamaker constant across a hydrocarbon layer is approximately 0.3 eV [19]. We assume that this value is general for semiconductors. The semiconductor-gold interaction can be derived (approximately) from these interactions using the relation[15] $A_{12} \approx \sqrt{A_1 A_2}$. Note that we assume no temperature dependence of the Hamaker constant. For a more complete discussion of the Hamaker constant, see Ref. 15.

B. Steric Interactions

To model the steric interaction, we use the Alexander-de Gennes model [15]. This model approximates the interaction between plates with an absorbed polymer layer in a good solvent with a high coverage of the polymer capping molecules. To transform this interaction between plates to an interaction between spheres of diameter σ_i and σ_j we use the Derjaguin approximation [15]. The resulting interaction between the spheres is given by

$$\beta V_{\rm steric}(r_{ij},\sigma_i,\sigma_j) = \begin{cases} \frac{32\pi S_{ij}L^2}{70s^3}\left[28(x_{ij}^{-1/4}-1)+\frac{20}{11}(1-x_{ij}^{11/4})+12(x_{ij}-1)\right] & r_{\rm c} < r_{ij} < r_{\rm c}+2L \\ 0 & \text{otherwise} \end{cases}$$

where $x_{ij} = D_{ij}/(2L)$, $r_c = (\sigma_1+\sigma_2)/2$, s is the mean distance between attachment points of the capping ligands (which we refer to as the ligand distance for the remainder of this paper) and L is the thickness of the capping layer. Here we have made the further approximation that the interaction length and ligand distance of the capping layer are the same for all nanoparticle mixtures. In reality, the ligand distance and thickness of the capping layer can be different between the various semiconductor and gold nanoparticles.

C. Study of Parameters

In this section we study the effect of particle radius, capping ligand distance and capping layer thickness on the effective semiconductor-semiconductor (SC-SC), gold-gold (Au-Au), and semiconductor-gold (SC-Au) interactions.

The various nanoparticles examined in this paper are capped with either dodecanethiol, or a combination of dodecathiol and oleic acid. The interaction length of dodecanethiol on a silver nanoparticle is $L \approx 1.5$ nm [20]. Oleid acid should have a slightly shorter interaction range. For the capping ligand distance, Ref. 20 measures a mean distance of $s \approx 0.43$ nm between the dodecanethiol ligands on a silver nanoparticle. Using these parameters we plot the effective SC-SC, Au-Au, and SC-Au interactions as a function of size ratio (Figs. S6, S7, and S8). We observe that since the VdWs interactions between the nanoparticles are weaker for smaller particles, the steric screening is generally more effective for the smaller particles. Similarly, the weaker VdWs interactions for SC-SC mixtures also result in more effective steric screening as compared to the SC-Au and particularly, Au-Au mixtures. In all cases, the effective interaction displays a strong short-range repulsion and longer-ranged, weak attraction of less than 3 k_BT.

In Figs. S9, S10 and S11, the effect of temperature on the various interaction types is examined. In all cases, the steric interaction screens the VdWs interactions better at higher temperatures. However, the temperature dependence of the screening is almost negligible in the SC-SC interactions which are well screened even at low temperature: the difference between the attraction over the full range of temperatures studied (150-390 K) is much less than 1 k_BT. In contrast, over the same temperature range, the attractive well of the Au-Au effective interactions ranges between approximately 2 to 6 k_BT indicating a much stronger role of temperature in the Au-Au interactions.

The effect of the capping layer thickness is examined in Figs. S12, S13, and S14. In general, the screening of the VdWs interactions is improved by increasing the capping layer thickness, however, the effect is much less important in the case of SC-SC interactions. While the variation of the attractive well for the SC-SC interactions is less than 0.5 k_BT in all cases, in the case of Au-Au effective interactions the well depth can be tuned from approximately 1 to 8 k_BT by varying the capping layer thickness between 2 and 1 nm. Additionally, the effective particle size is strongly effected by the thickness of the capping layer.

Finally, in Figs. S15, S16, and S17 the effect of ligand distance s is examined. Specifically, the effective interactions for SC-SC, Au-Au, and SC-Au nanoparticles is plotted for mean distances between ligand molecules between $s = 0.3 - 0.5$ nm. In general, the distance between the ligand molecules effects the softness of the short-range repulsion, but has no other significant effect in all cases.

In summary, the SC-SC effective interactions have little dependence on the capping layer details, with only slight variations in the softness of the short-range repulsion and attractive well depths never exceeding 1 k_BT over the complete range of parameters examined. Thus, in all cases it appears that the SC-SC interactions are well modelled by a hard-core repulsion, where the only relevant parameters are the relative size ratio between the radius of the particles and the composition of the mixture. The effective length of the capping ligands will effect the relative size ratio between the particles.

In contrast, the temperature, capping layer thickness, and particle size are found to largely effect the Au-Au effective interactions, and to a much smaller extent, the SC-Au interaction. Thus, in modelling SC-Au, or Au-Au mixtures, the details of the ligand coating is expected to be important in determining effective interactions, and, as a result, the resulting phase behaviour of the system.

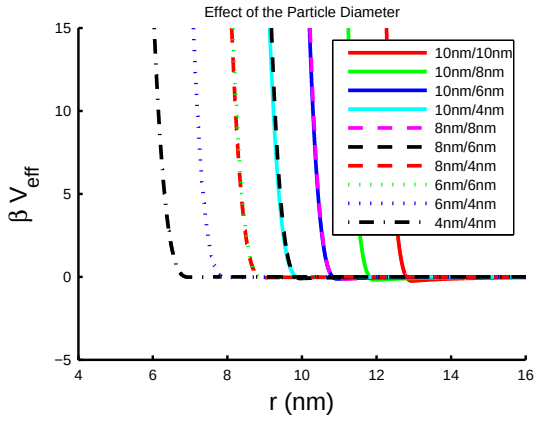

FIG. S6: Effective interactions between two semiconductor nanoparticles for particle diameters as labelled with Hamaker constant $A = 0.3$ eV, capping layer thickness $L = 1.5$ nm, and ligand distance $s = 0.43$ nm at temperature $T = 300$ K.

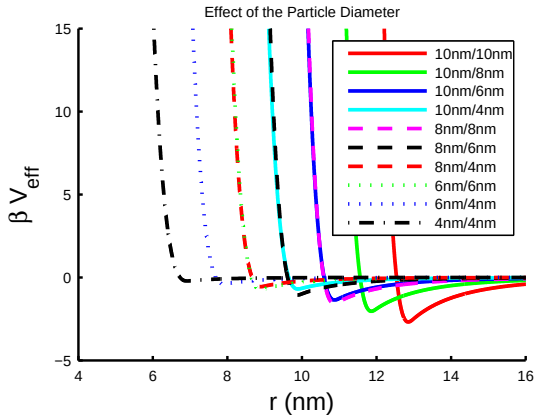

FIG. S7: Effective interactions between two gold nanoparticles for particle diameters as labelled with Hamaker constant $A = 3$ eV, capping layer thickness $L = 1.5$ nm, and ligand distance $s = 0.43$ nm at room temperature ($T = 300$ K).

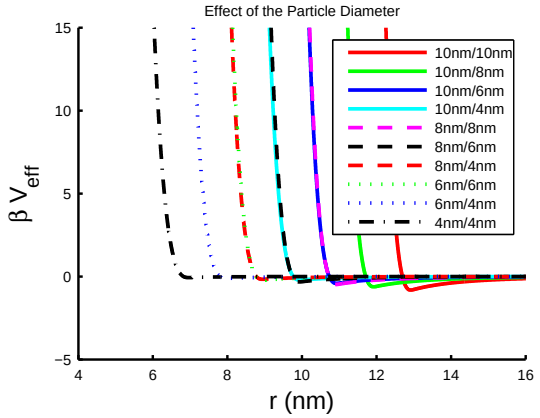

FIG. S8: Effective interaction between a semiconductor and a gold nanoparticle for particle diameters as labelled and with Hamaker constant $A = \sqrt{0.3 * 3.0}$ eV, capping layer thickness $L = 1.5$ nm, and ligand distance $s = 0.43$ nm at temperature $T = 300$ K.

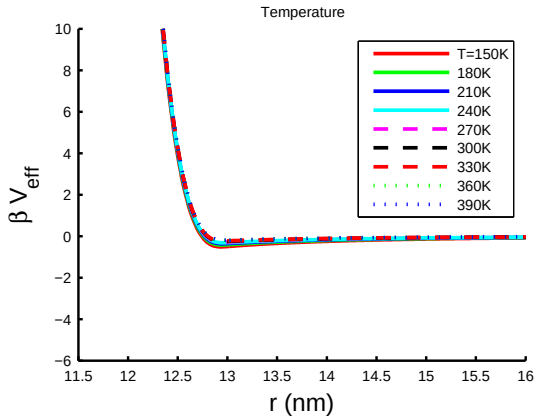

FIG. S9: Effective interactions between two 10 nm semiconductor nanoparticles for temperatures as labelled and with Hamaker constant $A = 0.3$ eV, capping layer thickness $L = 1.5$ nm, and ligand distance $s = 0.43$ nm.

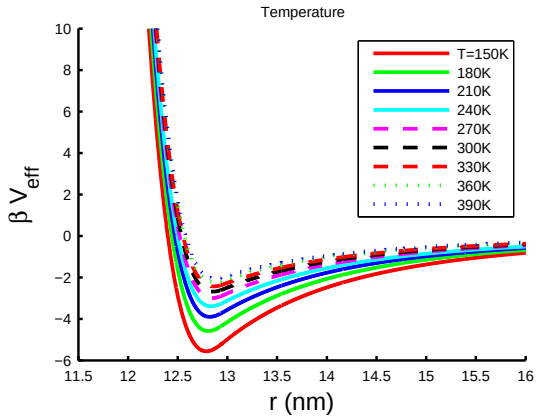

FIG. S10: Effective interactions between two 10 nm gold nanopaticles for temperatures as labelled with Hamaker constant $A = 3$ eV, capping layer thickness $L = 1.5$ nm, and ligand distance $s = 0.43$ nm.

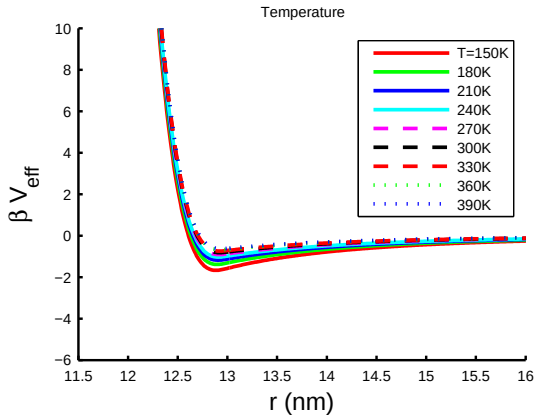

FIG. S11: Effective interactions between a semiconductor and a gold nanoparticle both with diameter 10 nm for temperatures as labelled and with Hamaker constant $A = \sqrt{0.3 * 3}$ eV, capping layer thickness $L = 1.5$ nm, and ligand distance $s = 0.43$ nm.

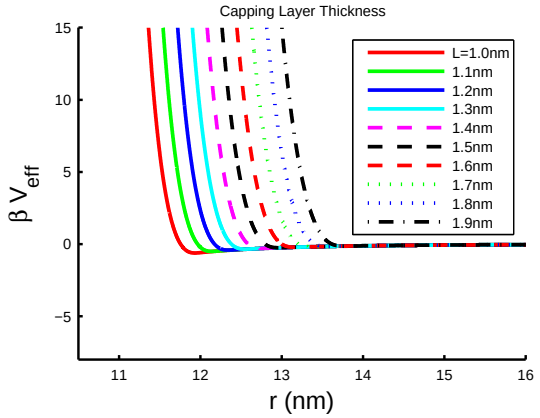

FIG. S12: Effective interactions between two 10 nm semiconductor nanoparticles for capping layer thicknesses L as labelled and with Hamaker constant $A = 0.3$ eV, and ligand distance $s = 0.43$ nm at temperature $T = 300$ K.

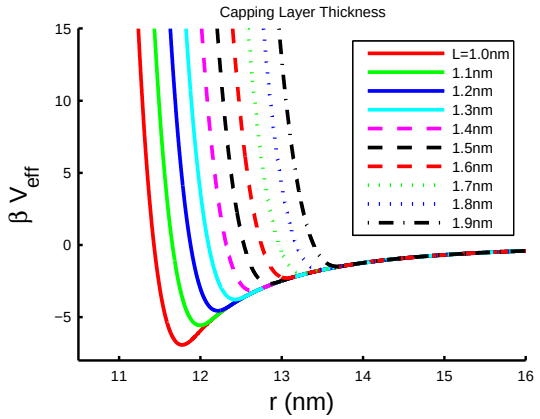

FIG. S13: Effective interactions between two 10 nm gold nanoparticles for capping layer thicknesses L as labelled and with Hamaker constant $A = 3$ eV, and ligand distance $s = 0.43$ nm at temperature $T = 300$ K.

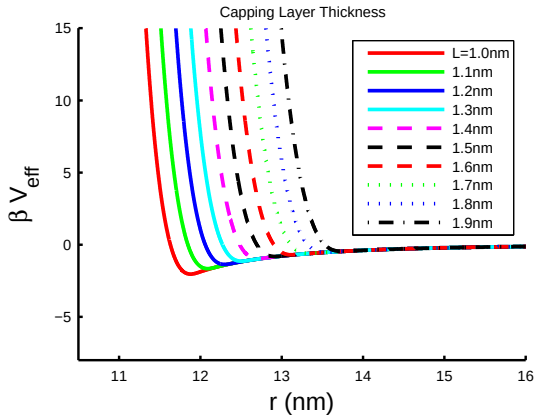

FIG. S14: Effective interactions between a 10 nm semiconductor nanoparticle and a 10nm gold nanoparticle for capping layer thicknesses L as labelled with Hamaker constant $A = \sqrt{3 * 0.3}$ eV, and ligand distance $s = 0.43$ nm at temperature $T = 300$ K.

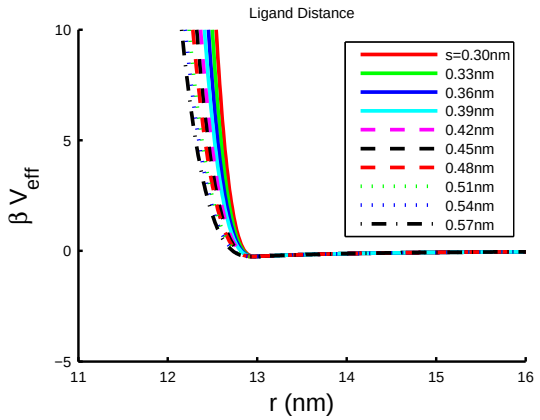

FIG. S15: Effective interactions between two 10 nm semiconductor nanoparticles for capping layer densities s as labelled with Hamaker constant $A = 0.3$ eV, and capping layer thickness $L = 1.5$ nm at temperature $T = 300$ K.

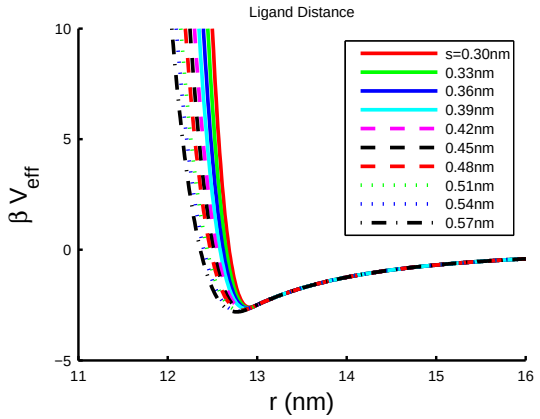

FIG. S16: Effective interactions between two 10 nm gold nanoparticles for capping layer densities s as labelled with Hamaker constant $A = 3$ eV, and capping layer thickness $L = 1.5$ nm at temperature $T = 300$ K

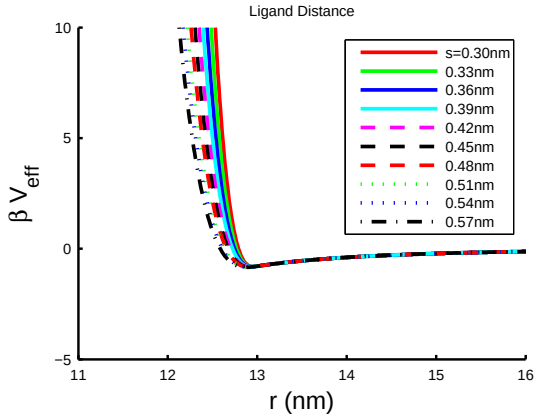

FIG. S17: Effective interactions between a 10 nm semiconductor nanoparticle and a 10 nm gold nanoparticle for capping layer densities s as labelled with Hamaker constant $A = \sqrt{3 * 0.3}$ eV, and capping layer thickness $L = 1.5$ nm at temperature $T = 300$ K.

[1] M. Dijkstra, R. van Roij, and R. Evans, Phys. Rev. E **59**, 5744 (1999).
[2] E. Trizac, M. D. Eldridge, and P. A. Madden, Mol. Phys. **90**, 675 (1997).
[3] M. D. Eldridge, P. A. Madden, P. N. Pusey, and P. Bartlett, Mol. Phys. **84**, 395 (1995).
[4] M. D. Eldridge, P. A. Madden, and D. Frenkel, Nature **365**, 35 (1993).
[5] A. Hynninen, L. Filion, and M. Dijkstra, J. Chem. Phys. **131**, 064902 (2009).
[6] W. Kranendonk and D. Frenkel, Mol. Phys. **72**, 679 (1991).
[7] D. Frenkel and B. Smit, *Understanding Molecular Simulation: From Algorithms to Applications* (Academic Press, San Diego, 1996).
[8] J. M. Polson, E. Trizac, S. Pronk, and D. Frenkel, J. Chem. Phys **112**, 5339 (2000).
[9] R. J. Speedy, J Phys. Cond. Mat. **10**, 4387 (1998).
[10] B. Derjaguin and L. Landau, Acta Physicochim. URSS **14**, 633 (1941).
[11] E. J. W. Verwey and J. T. Overbeek, *Theory of the stability of lyophobic colloids* (Elsevier, Amsterdam, 1948).
[12] C. N. Likos, Physics Reports **348**, 267 (2001).
[13] E. V. Shevchenko, D. V. Talapin, C. B. Murray, and S. O'Brien, J. Am. Chem. Soc. **128**, 3620 (2006).
[14] P. C. Ohara, D. V. Leff, J. R. Heath, and W. M. Gelbart, Phys. Rev. Lett **75**, 3466 (1995).
[15] J. Israelachvili, *Intermolecular and Surface Forces* (Academic Press, London, 1992).
[16] P. S. Shah, J. D. Holmes, K. P. Johnston, and B. A. Korgel, J. Phys. Chem. B **106**, 2545 (2002).
[17] A. E. Saunders and B. A. Korgel, J. Phys. Chem. B **108**, 16732 (2004).
[18] D. Bargeman and F. van Voorst Vader, J. Electroanal. Chem. **37**, 45 (1972).
[19] G. Ge and L. Brus, J. Phys. Chem. B **104**, 9573 (2000).
[20] B. A. Korgel, S. Fullam, S. Connolly, and D. Fitzmaurice, J. Phys. Chem. B **102**, 8379 (1998).